

AD_____

Award Number: W81XWH-05-1-0363

TITLE: Minature and Molecularly Specific Optical Screening Technologies for Breast Cancer

PRINCIPAL INVESTIGATOR: Dr. Nirmala Ramanujam

CONTRACTING ORGANIZATION: Duke University
Durham, NC 27708

REPORT DATE: October 2007

TYPE OF REPORT: Annual

PREPARED FOR: U.S. Army Medical Research and Materiel Command
Fort Detrick, Maryland 21702-5012

DISTRIBUTION STATEMENT: Approved for Public Release;
Distribution Unlimited

The views, opinions and/or findings contained in this report are those of the author(s) and should not be construed as an official Department of the Army position, policy or decision unless so designated by other documentation.

REPORT DOCUMENTATION PAGE				Form Approved OMB No. 0704-0188	
Public reporting burden for this collection of information is estimated to average 1 hour per response, including the time for reviewing instructions, searching existing data sources, gathering and maintaining the data needed, and completing and reviewing this collection of information. Send comments regarding this burden estimate or any other aspect of this collection of information, including suggestions for reducing this burden to Department of Defense, Washington Headquarters Services, Directorate for Information Operations and Reports (0704-0188), 1215 Jefferson Davis Highway, Suite 1204, Arlington, VA 22202-4302. Respondents should be aware that notwithstanding any other provision of law, no person shall be subject to any penalty for failing to comply with a collection of information if it does not display a currently valid OMB control number. PLEASE DO NOT RETURN YOUR FORM TO THE ABOVE ADDRESS.					
1. REPORT DATE (DD-MM-YYYY) 01-OCT-2007		2. REPORT TYPE Annual		3. DATES COVERED (From - To) 1 SEP 2006 - 31 AUG 2007	
4. TITLE AND SUBTITLE Minature and Molecularly Specific Optical Screening Technologies for Breast Cancer				5a. CONTRACT NUMBER	
				5b. GRANT NUMBER W81XWH-05-1-0363	
				5c. PROGRAM ELEMENT NUMBER	
6. AUTHOR(S) Dr. Nirmala Ramanujam E-Mail: nimmi@duke.edu				5d. PROJECT NUMBER	
				5e. TASK NUMBER	
				5f. WORK UNIT NUMBER	
7. PERFORMING ORGANIZATION NAME(S) AND ADDRESS(ES) Duke University Durham, NC 27708				8. PERFORMING ORGANIZATION REPORT NUMBER	
9. SPONSORING / MONITORING AGENCY NAME(S) AND ADDRESS(ES) U.S. Army Medical Research and Materiel Command Fort Detrick, Maryland 21702-5012				10. SPONSOR/MONITOR'S ACRONYM(S)	
				11. SPONSOR/MONITOR'S REPORT NUMBER(S)	
12. DISTRIBUTION / AVAILABILITY STATEMENT Approved for Public Release; Distribution Unlimited					
13. SUPPLEMENTARY NOTES					
14. ABSTRACT The goal of this proposal is to harness the power of light to create "miniature and molecularly specific optical technologies" for breast cancer diagnosis and detection. The miniature technologies will leverage on millimeter scale silicon detectors and LEDs to make compact devices that can be used in a practical clinical setting for breast cancer detection. The features that will be exploited for optical detection/diagnosis of breast cancer will include the physiological, structural and molecular alterations that accompany the transformation of a cell from a normal to malignant state. This proposal also focuses on using contrast agents, specifically aminolevulinic acid (ALA) induced protoporphyrin IX (PpIX), for the molecular detection of breast cancer.					
15. SUBJECT TERMS optical, spectroscopy, imaging, fiber-optic, molecular, screening					
16. SECURITY CLASSIFICATION OF:			17. LIMITATION OF ABSTRACT	18. NUMBER OF PAGES 40	19a. NAME OF RESPONSIBLE PERSON USAMRMC
a. REPORT	b. ABSTRACT	c. THIS PAGE			19b. TELEPHONE NUMBER (include area code)

Table of Contents

INTRODUCTION	4
BODY	4
KEY RESEARCH ACCOMPLISHMENTS	18
REPORTABLE OUTCOMES	19
CONCLUSIONS	19
REFERENCES	20
APPENDIX	21

1. INTRODUCTION

The goal of this proposal is to harness the power of light to create “miniature and molecularly specific optical technologies” for breast cancer diagnosis and detection. The miniature technologies will leverage on millimeter scale silicon detectors and LEDs to make compact devices that can be used in a practical clinical setting for breast cancer detection. The features that will be exploited for optical detection/diagnosis of breast cancer will include the physiological, structural and molecular alterations that accompany the transformation of a cell from a normal to malignant state. This proposal also focuses on using contrast agents, specifically aminolevulinic acid (ALA) induced protoporphyrin IX (PpIX), for the molecular detection of breast cancer.

2. BODY

2.1 Project 1: System-on-a-chip device

The goal is to build a miniature device that can perform diffuse reflectance spectroscopy of breast tissues in the visible spectral range between 350-600 nm. The measured spectra will be processed using an inverse Monte Carlo (MC) model to extract optical properties (absorption and scattering) which reflect the physiological (total hemoglobin content and hemoglobin saturation) and structural properties of breast tissues.

In year 1, we have completed thermal modeling of the heat dissipation effects of compact LEDs on tissue samples, selection of multi-wavelength compact light sources, calculating bandwidth effects of broadband light sources (such as LEDs) on the RMS errors for the extracted tissue optical properties, selection of photodiodes, and the design and testing of various single-pixel probe prototypes (P1 and P2 as shown in Figure 1).

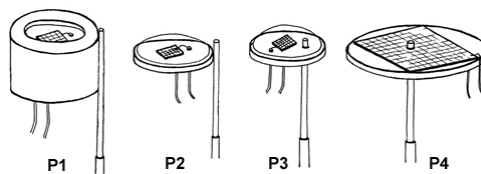


Figure 1. Conceptual drawings of four single-pixel probe geometries P1-P4.

Statement of work for year 2

To engineer and test the first-generation system-on-a-chip device. The knowledge base derived from aim 1 will be used to engineer a first generation system-on-a-chip device and the performance of the device will be characterized on synthetic tissue phantom models.

Like the bench-top system, the system-on-a-chip device will be able to measure the underlying physiological and morphological properties of breast tissue. Consisting of light-emitting diodes and a silicon photodetector, the device will be significantly smaller in size than the bench-top system, which consists of a xenon lamp, a monochromator, a optic fiber probe, a spectrograph, and a CCD camera. The signal-to-noise ratio (SNR) and reflectance characteristics of the system-on-a-chip device will be compared to that of a standard bench-top counterpart (year 2).

Accomplishments in year 2

This section describes the research accomplishments associated with each task outlined in the above Statement of Work (SOW). We have built single-pixel probes of different illumination and detection

geometries named as P3-1, P3-2, P4-1, and P4-2 (as shown in Figure 1). P3-1 and P3-2 were tested in synthetic tissue phantoms with known optical properties, and their experimental diffuse reflectance spectra were compared with those of a forward Monte Carlo model. We have also extracted phantom optical properties from the diffuse reflectance spectra obtained from a tunable light source using an inverse Monte Carlo model [1]. Phantom optical properties with reduced number of wavelengths were also extracted and compared to that of the bench-top system with all wavelengths. Lastly, a first generation system-on-a-chip single channel device was designed and built.

2.1.1. Optical spectral imaging system based on tunable source and silicon detector

Although our final goal is to build a system-on-a-chip imaging system for cancer diagnosis and tumor margin assessment, we understand that many challenges exist and it may take a relatively long time to reach this goal. As an intermediate step, it is also significant if we can partially miniaturize the current bench-top system. For example, replace the current spectrograph and CCD based detection system with a single photodiode (P1 to P4 as shown in Figure 1). This miniaturized probe preserves the potential for multiplexing that can be used for spectral imaging of tissue while uses all the wavelengths available to the bench-top system.

A. Single-pixel probe design and fabrication

In year 1, we designed and tested single-pixel probes P1 and P2 and found that the fiber-to-detector separation needs to be minimized and that the uncut $1 \times 1 \text{ mm}^2$ photodetector (Hamamatsu S1226-18B) coupled with a $600\text{-}\mu\text{m}$ fiber does not give sufficient signal for tissue phantoms with high absorption coefficients. The first iteration of P3 (P3-1) was to trim the edge off of the base of the photodetector so that we can bring the fiber as close to the detector as possible to maximize the signal. The next iteration for P3 (P3-2) was to increase the photodetector area and illumination fiber diameter, thus increasing the signal of the system. P3-2 was built with a $2.4 \times 2.4 \text{ mm}^2$ detector (Hamamatsu S1226-5B) with an edge trimmed and a fiber with a 1 mm diameter adjacent to the detector. Experimental setup and results are presented in the next section. In addition to the P3-1 and P3-2 designs, we have also built two P4 probes, P4-1 and P4-2. These probes are made with Hamamatsu S1227 photodetectors, which have a $2.4 \times 2.4 \text{ mm}^2$ active area with a hole drilled in the center of the detector. P4-1 has a $600 \text{ }\mu\text{m}$ diameter fiber fitted through the hole in the center of the detector while P4-2 has a 1-mm diameter fiber in the center. P4-1 and P4-2 will also be tested in liquid phantoms once we have an accurate model for their respective geometries. We expect P4-1 and P4-2 to have a higher SNR because the fiber-to-detector (center-to-center) distance is near zero.

B. Single-pixel probe experiments

We made 16 liquid phantoms (A1-D4) that mimicked tissue optical properties using 20% intralipid (scatterer) and ink (absorber). The optical properties of the 16 phantoms are listed in the second column in Table 1. Diffuse reflectance measurements were made by coupling a single wavelength of 660 nm from a laser diode into the $600 \text{ }\mu\text{m}$ fiber of P3-1. The total optical power delivered to the liquid phantom was about 1.0 mW. A forward MC model was used to obtain a simulated diffuse reflectance at 660 nm for each phantom (with known optical properties). The simulated data and the measured data were both normalized to the phantom with the lowest absorption and highest scattering, which generated the highest diffuse reflectance among all the 16 phantoms. The ratio of the normalized measured data to the normalized simulated data should be approximately equal to 1 if the forward model is valid. Table 1 shows the comparison of the measured and simulated results for P3-1. The optical properties, μ_a (absorption coefficient) and μ_s (scattering coefficient), are within the range of those of breast tissue. The table shows that for this specific wavelength (660 nm), the measured data matches the simulated data very well, and therefore it is possible to apply an inverse MC model through all wavelengths of interest (400-600 nm) to extract the phantom optical properties.

Table 1. Comparison of measured and forward-simulated results for P3-1 at 660 nm.

Phantom #	Properties (μ_a , μ_s')	Sim Norm	Measured Norm	Measured/Sim
A1	0.1132, 5.04	0.4136	0.4277	1.03
B1	0.1132, 8.41	0.6985	0.6515	0.93
C1	0.1132, 12.33	0.8518	0.8802	1.03
D1	0.1132, 16.82	1.0000	1.0000	1.00
A2	1.2014, 5.03	0.2576	0.3129	1.21
B2	1.2014, 8.39	0.4441	0.4396	0.99
C2	1.2014, 12.3	0.5429	0.5624	1.04
D2	1.2014, 16.77	0.7456	0.6178	0.83
A3	6.7734, 4.97	0.0606	0.0806	1.33
B3	6.7734, 8.28	0.1095	0.1277	1.17
C3	6.7734, 12.14	0.1550	0.1840	1.19
D3	6.7734, 16.56	0.1875	0.2139	1.14
A4	15.0725, 4.87	0.0183	0.0238	1.30
B4	15.0725, 8.12	0.0251	0.0345	1.37
C4	15.0725, 11.91	0.0356	0.0481	1.35
D4	15.0725, 16.24	0.0414	0.0489	1.18

The next step was to test the probe using a tunable light source so that all 41 wavelengths can be utilized (currently used in the bench-top system) from 400 to 600 nm in 5 nm increments. It was found that while we obtained sufficient signal at 660 nm (using a laser diode), the detector was not sensitive enough for darker phantoms when we attempted to make measurements at the shortest and longest wavelengths using a tunable light source (xenon lamp and monochromator). Thus, P3-2 was made with a larger detector ($2.4 \times 2.4 \text{ mm}^2$ vs. 1 mm^2) and a larger fiber (1-mm diameter vs. 600- μm diameter), which resulted in 10 times more signal than that of P3-1 under same conditions. The probe is still small enough that we do not compromise the goal of miniaturization, yet we also obtain much higher sensitivity.

With probe P3-2, we preformed a set of initial phantom experiments and MC inversions to obtain the optical properties to compare with the known optical properties of the liquid phantoms. Polystyrene spheres were used as the scatterer and hemoglobin was used as the absorber in the liquid phantoms. Table 2 shows the set of 10 phantoms used in the experiment with varying absorption and reduced scattering coefficients that are common in normal breast tissue. We used the tunable source to couple light into the fiber of P3-2 and collected data from 400-600 nm, similar to the methods used in previous studies with the bench-top system. Tables 3 and 4 show the percent inversion errors for the two optical properties, μ_s' and μ_a . Phantoms 2D and 1E were taken out of the results due to experimental error. The first row of the table refers to the reference phantoms, and the first column denotes the target phantoms. The overall average error for the reduced scattering coefficient is 22.85% and for the absorption coefficient is 16.51%. In a previous study on the MC-based inverse model for calculating tissue optical properties with phantom validations [2], the mean RMS errors obtained were in the 5% range. The measurements in the previous study were done with a large, bench-top system. While our initial inversion results are not as good as those from a manufactured clinical instrument, we feel confident that we will be able to minimize these inversion errors by doing more work to understand the detector characteristics.

Table 2. Liquid phantoms and corresponding optical properties.

Phantoms #	μ_a (1/cm ³)	μ_s' (1/cm ³)
1A	0.5	13.17
1B	0.9	12.95
1C	1.3	12.73
1D	1.6	12.56
1E	2.0	12.33
2A	0.5	22.96
2B	0.9	22.57
2C	1.3	22.18
2D	1.6	21.89
2E	2.0	21.50

Table 3. MC inversion errors (%) for reduced scattering coefficients.

μ_s'	1A	1B	1C	1D	2A	2B	2C	2E	
1A	0.00	8.05	8.24	27.75	7.41	19.86	32.39	18.74	
1B	15.65	0.00	3.93	36.66	4.31	17.92	34.52	26.29	
1C	41.27	32.33	0.00	42.46	9.11	24.56	39.04	42.38	
1D	20.69	23.93	37.89	0.00	34.04	7.46	5.27	15.23	
2A	6.67	9.31	2.36	9.97	0.00	16.52	13.67	9.81	
2B	68.15	63.74	73.69	9.39	75.32	0.00	5.18	50.69	
2C	12.68	8.21	52.92	4.47	38.13	19.46	0.00	8.59	
2E	38.36	41.61	55.75	3.41	51.95	41.40	33.86	0.00	
Avg Error	25.43	23.40	29.35	16.76	27.53	18.40	20.49	21.46	22.85

Table 4. MC inversion errors (%) for absorption coefficients.

μ_a	1A	1B	1C	1D	2A	2B	2C	2E	
1A	0.00	2.94	3.81	8.28	5.35	28.95	91.69	19.94	
1B	15.63	0.00	16.76	11.64	25.87	9.70	18.63	3.50	
1C	4.87	2.36	0.00	19.35	19.97	8.72	4.59	8.83	
1D	0.77	9.69	11.12	0.00	6.95	7.83	9.39	4.79	
2A	16.42	9.14	13.80	17.10	0.00	22.62	81.95	24.60	
2B	36.62	37.07	35.78	8.72	21.88	0.00	74.23	28.86	
2C	48.83	37.33	19.41	3.06	48.30	9.11	0.00	17.55	
2E	15.22	3.18	5.81	8.59	15.55	8.72	5.42	0.00	
Avg Error	17.29	12.71	13.31	9.59	17.98	11.96	35.74	13.51	16.51

To further understand the sources of these inversion errors of P3-2, we performed forward modeling on several wavelengths for the measured data (Table 5). Again, to show the accuracy of the MC forward model compared to the measured data, the measured to simulated ratio should be near 1. For the wavelengths 500 and 560 nm, there is good agreement between the simulated and measured data. However, for the 400 and 420 nm wavelengths, there is not good agreement between the data. This could be due to the low signal at shorter wavelengths (due to the high hemoglobin absorption around 420 nm) that is affecting the current amplifier measurements.

Table 5. Comparison of measured and MC simulation forward model data at various wavelengths.

400 nm	Measured	Measured (Normalized)	Simulated	Simulated (Normalized)	Measured/Simulated (Normalized)
1A	0.3682	1.00	0.0095	1.00	1.00
1B	0.2241	0.61	0.0072	0.76	0.80
1C	-0.0409	-0.11	0.0056	0.59	-0.19
1D	0.1113	0.30	0.0048	0.51	0.60
2A	0.3334	0.91	0.0169	1.78	0.51
2B	0.1949	0.53	0.0129	1.36	0.39
2C	0.0577	0.16	0.0102	1.07	0.15
2E	0.0538	0.15	0.0065	0.68	0.21

420 nm	Measured	Measured (Normalized)	Simulated	Simulated (Normalized)	Measured/Simulated (Normalized)
1A	0.3227	1.00	0.0097	1.00	1.00
1B	-0.0912	-0.28	0.0073	0.75	-0.38
1C	0.0550	0.17	0.0058	0.59	0.29
1D	-0.0261	-0.08	0.0048	0.50	-0.16
2A	0.3135	0.97	0.0171	1.76	0.55
2B	0.1603	0.50	0.0132	1.35	0.37
2C	-0.1212	-0.38	0.0103	1.06	-0.35
2E	0.0415	0.13	0.0071	0.73	0.18

500 nm	Measured	Measured (Normalized)	Simulated	Simulated (Normalized)	Measured/Simulated (Normalized)
1A	1.1453	1.00	0.0098	1.00	1.00
1B	1.0409	0.91	0.0084	0.85	1.06
1C	1.0367	0.91	0.0067	0.69	1.32
1D	0.8600	0.75	0.0058	0.60	1.26
2A	1.1889	1.04	0.0108	1.10	0.94
2B	1.0326	0.90	0.0103	1.05	0.86
2C	0.9200	0.80	0.0087	0.89	0.90
2E	0.8518	0.74	0.0071	0.73	1.02

560 nm	Measured	Measured (Normalized)	Simulated	Simulated (Normalized)	Measured/Simulated (Normalized)
1A	0.7766	1.00	0.0099	1.00	1.00
1B	0.6575	0.85	0.0074	0.75	1.12
1C	0.6961	0.90	0.0068	0.69	1.30
1D	0.4297	0.55	0.0048	0.49	1.13
2A	0.8356	1.08	0.0119	1.21	0.89
2B	0.6931	0.89	0.0100	1.01	0.88
2C	0.5815	0.75	0.0099	1.00	0.75
2E	0.5195	0.67	0.0071	0.72	0.93

We also performed repeatability experiments using the P3-2 probe. One highly scattering non-absorbing liquid phantom made with pure polystyrene spheres was used for the study. The xenon lamp was allowed to warm-up for 20 minutes prior to the first scan of 400-600 nm. Repeated scans were made at the 15, 30, 45, and 60 minute marks to verify if the spectra would be the same. Figure 2 shows excellent repeatability for this particular phantom.

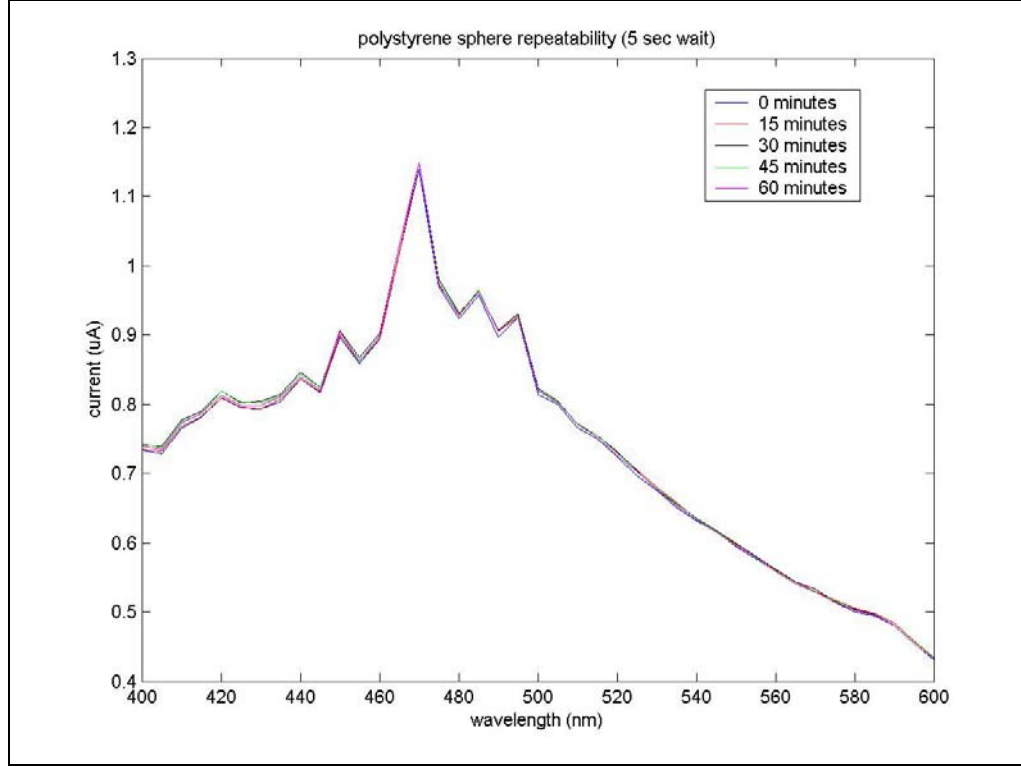


Figure 2. Phantom measurement repeatability study over 1 hour period.

2.1.2. System-on-a-chip spectral imaging system

Here we aim to replace the white light source and the monochromator in the bench-top system with LEDs to make the system truly compact. This requires reducing the number of wavelengths to a practical number that can be provided by LEDs.

A. Wavelength reduction

In year 1, we carried out a series of Monte Carlo simulations to evaluate the effects of the reduced number of wavelengths and increased bandwidth on the accuracy with which optical properties and hemoglobin content and saturation can be extracted. In year 2 we conducted phantom experiments to test the effects of reducing the number of wavelengths from 41 (400 - 600 nm in 5 nm increments) to 5 (420, 440, 475, 540 and 560 nm). 10 liquid tissue phantoms of two absorption levels (A - 0.9 cm^{-1} and B - 1.6 cm^{-1}) were made using Hemoglobin as the absorber, Polystyrene sphere as scatterer, and water and by scattering titration. The average expected reduced scattering coefficients (μ_s') and absorption coefficients (μ_a) over the wavelength range of 350-800 nm are given in Table 6.

The diffuse reflectance spectrum was obtained from each of the ten test phantoms using the current bench-top system and a fiber optic probe [2]. An inverse Monte Carlo algorithm, developed by our laboratory, was used to extract the absorption and reduced scattering properties of the test phantoms from the recorded

spectra. In each inversion, one of the ten phantoms was used as a reference phantom and the remaining phantoms were treated as targets. The accuracy with which phantom optical properties can be extracted is represented by the percent root mean squared error (RMSE):

$$\text{RMSE}_{\mu a} = (1/N) * [\sum (\mu a_{\text{extracted}}(\lambda_i) - \mu a_{\text{expected}}(\lambda_i))^2 / \mu a_{\text{expected}}(\lambda_i)^2]^{1/2} \quad (1)$$

$$\text{RMSE}_{\mu s'} = (1/N) * [\sum (\mu s'_{\text{extracted}}(\lambda_i) - \mu s'_{\text{expected}}(\lambda_i))^2 / \mu s'_{\text{expected}}(\lambda_i)^2]^{1/2} \quad (2)$$

Where N is the total number of wavelength (41 for the bench-top system and 5 for the miniature device). Table 7 shows the RMSE of μa and $\mu s'$ over the wavelength range of 400 – 600 nm, where the phantom at the top row indicates the reference phantom. As shown in Table 7, the overall RMSE error was 8.21% for μa and 4.26% for $\mu s'$ for 41 wavelengths (400:5:600 nm), and 7.31% and 4.52% for 5 wavelengths (420, 440, 475, 540 and 560 nm), respectively. No noticeable increase of RMSE errors was observed. These results indicate that the spectral data obtained using a five-wavelength based device can be used for extraction of optical properties using algorithms developed for the bench-top system.

Table 6. Expected phantom optical properties from 350-800 nm.

Phantom #	Average Expected $\mu s'$ (1/cm, 350-800 nm)	Average Expected μa (1/cm, 350-800 nm)
1A	8.90	0.90
2A	13.30	0.85
3A	17.80	0.80
4A	22.20	0.75
5A	26.70	0.70
1B	8.90	1.60
2B	13.30	1.51
3B	17.80	1.42
4B	22.20	1.33
5B	26.70	1.24

Table 7. Percent RMSE of the extracted optical properties over expected optical properties.

Percent RMSE μa			400:5:600 nm									
	1A	2A	3A	4A	5A	1B	2B	3B	4B	5B	Ave	
1A	0.00	5.89	9.93	0.41	13.96	2.42	6.38	9.62	10.61	14.83	7.40	
2A	5.69	0.00	2.99	5.91	9.24	19.70	0.02	16.75	3.54	0.81	6.46	
3A	20.62	3.96	0.00	8.83	4.77	21.56	11.31	8.71	2.04	1.92	8.37	
4A	20.24	12.42	1.87	0.00	3.90	23.18	9.99	12.19	0.11	7.16	9.11	
5A	27.40	17.59	14.59	13.56	0.00	31.36	16.84	24.59	10.65	6.45	16.30	
1B	3.00	3.34	0.41	6.99	11.38	0.00	7.05	1.73	5.95	11.27	5.11	
2B	7.37	0.97	6.51	0.20	5.70	6.49	0.00	5.81	1.95	5.63	4.06	
3B	9.10	4.66	7.27	7.72	9.93	4.39	3.63	0.00	7.91	10.41	6.50	
4B	15.85	11.39	0.82	0.26	4.26	20.99	11.09	9.36	0.00	3.32	7.73	
5B	22.28	13.89	5.15	3.39	0.58	25.60	14.17	20.52	4.36	0.00	10.99	
Ave	13.15	7.41	4.95	4.73	6.37	15.57	8.05	10.93	4.71	6.18	8.21	
Percent RMSE $\mu s'$			400:5:600 nm									

	1A	2A	3A	4A	5A	1B	2B	3B	4B	5B	Ave
1A	0.00	3.17	6.94	4.23	2.41	1.94	2.72	3.73	4.60	1.85	3.16
2A	5.65	0.00	1.67	4.67	3.86	11.62	1.99	7.96	2.39	9.19	4.90
3A	9.98	1.34	0.00	5.65	6.69	12.12	6.33	5.23	2.99	11.86	6.22
4A	7.92	2.79	1.46	0.00	6.03	11.02	4.00	4.63	2.51	7.99	4.83
5A	2.69	6.19	5.90	4.07	0.00	5.36	4.06	2.31	3.22	6.46	4.03
1B	2.11	5.61	5.60	6.25	3.89	0.00	4.85	2.69	4.75	2.61	3.84
2B	3.98	2.22	3.43	2.17	2.44	5.82	0.00	2.67	1.37	3.96	2.80
3B	5.57	4.02	4.96	3.89	1.60	5.28	1.83	0.00	2.00	3.01	3.22
4B	6.76	2.31	3.72	2.31	7.49	11.51	3.95	2.67	0.00	9.74	5.04
5B	2.37	6.89	9.08	7.85	2.27	4.90	4.82	2.14	5.51	0.00	4.58
Ave	4.70	3.45	4.27	4.11	3.67	6.96	3.45	3.40	2.93	5.67	4.26
Percent RMSE $\mu\alpha$			420, 440, 475, 540, 560 nm								
	1A	2A	3A	4A	5A	1B	2B	3B	4B	5B	Ave
1A	0.36	0.15	0.20	6.73	5.45	3.07	0.04	2.96	2.25	11.83	3.31
2A	12.90	0.00	4.22	4.81	0.17	10.03	0.29	14.06	3.56	8.35	5.84
3A	10.76	2.59	0.00	8.44	2.95	16.27	8.59	15.26	3.17	0.06	6.81
4A	14.80	5.34	0.15	0.00	6.65	18.77	5.94	18.74	2.35	8.55	8.13
5A	21.28	10.17	10.48	12.71	0.68	26.84	11.55	25.09	2.61	5.01	12.64
1B	5.83	0.02	3.20	5.49	10.63	7.49	2.09	0.96	9.92	11.91	5.75
2B	12.25	7.58	5.52	2.96	0.03	7.81	0.00	9.76	4.72	5.99	5.66
3B	2.69	4.59	5.38	8.79	11.59	6.87	3.68	1.11	9.36	10.54	6.46
4B	16.75	10.21	8.42	3.56	4.90	16.19	9.92	12.43	0.00	1.89	8.43
5B	18.82	9.52	5.49	4.16	2.21	24.31	10.89	20.43	4.33	0.26	10.04
Ave	11.65	5.02	4.31	5.77	4.53	13.76	5.30	12.08	4.23	6.44	7.31
Percent RMSE $\mu s'$			420, 440, 475, 540, 560 nm								
	1A	2A	3A	4A	5A	1B	2B	3B	4B	5B	Ave
1A	0.29	3.40	4.74	3.81	4.35	2.56	2.33	1.54	4.53	2.11	2.97
2A	8.44	0.00	2.82	4.86	7.88	8.40	2.32	7.31	4.21	6.15	5.24
3A	7.06	1.33	0.00	6.02	9.91	11.05	5.91	7.21	4.42	10.66	6.36
4A	6.61	1.32	2.27	0.00	4.10	8.88	2.37	7.50	0.86	5.34	3.92
5A	1.14	7.56	6.60	3.36	0.57	5.13	4.28	2.21	5.97	5.44	4.22
1B	3.29	4.85	6.68	6.44	3.30	4.65	3.61	3.61	6.94	2.81	4.62
2B	7.95	3.34	3.36	3.78	6.00	6.89	0.00	4.77	3.05	3.72	4.29
3B	3.01	3.89	4.45	5.39	1.87	6.78	1.59	0.73	5.21	4.03	3.69
4B	9.68	2.96	2.91	1.58	9.27	10.97	5.10	5.24	0.00	6.78	5.45
5B	1.43	7.61	8.91	6.97	0.70	6.27	4.27	2.10	6.19	0.39	4.48
Ave	4.89	3.62	4.27	4.22	4.80	7.16	3.18	4.22	4.14	4.74	4.52

B. Development of a single-pixel device

Several probe designs have been considered and implemented according to the basic design over the last year. These probes are based on high-brightness LEDs and commercially available, small package, Si photodiodes. The LEDs were donated by LUMILEDs, Inc for this program and are partially mounted LEDs (shown in Figure 3). These LEDs can run up to 1 A of current (conventional LEDs run at ~20mA) provided adequate heat sinking. Hence there is a large potential dynamic range in intensity. The LED wavelengths at present are centered at 420, 440, 475, 540 and 560 nm.

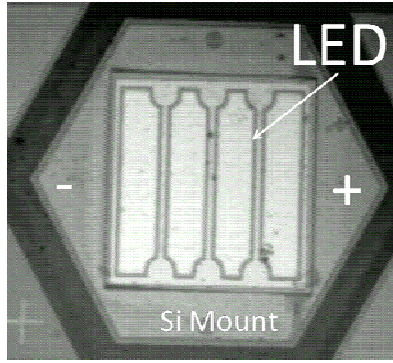


Figure 3. LUMILED LED and silicon submount used in probe fabrication with typical characteristics.

The Si photodiodes were obtained from the Hamamatsu and processed (such as demounting, for use in our systems). The performance specifications are shown in Figures 4 and 5. Figure 5 is an enlargement of the spectral region of interest. All three designs have been used. S1226 consists of a $1 \times 1 \text{ mm}^2$ nominal active, S1227 has a nominal $2.4 \times 2.4 \text{ mm}^2$ active area and the S6931 structure has a $2.4 \times 2.8 \text{ mm}^2$ active area. These photodiodes are square (or close to square) with a backside contact and a front side wire bond. The geometries of the detectors are shown in Figure 6. S6931 is a surface mount detector which could potentially simplify probe design and implementation.

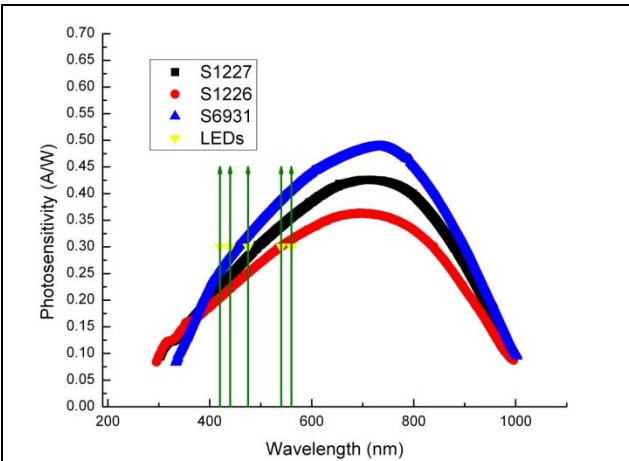


Figure 4. Detector performance comparison.

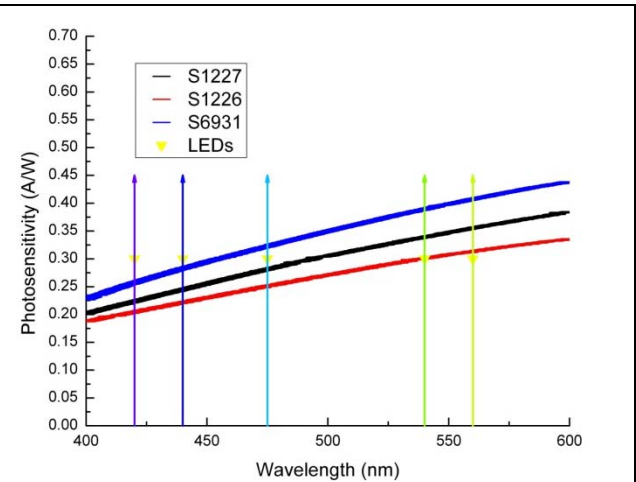


Figure 5. Detailed performance over spectral region of interest with LED wavelengths noted.

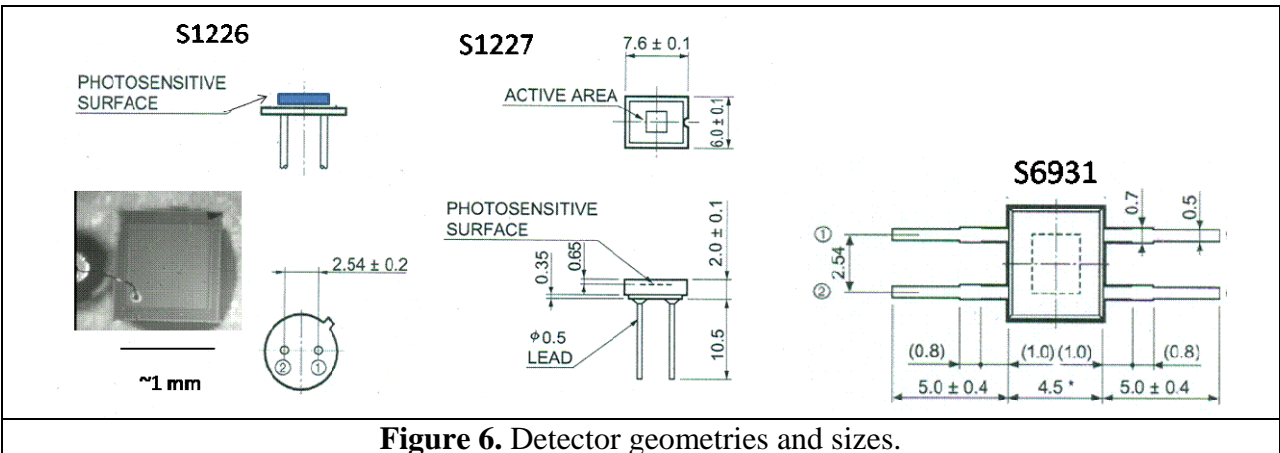


Figure 6. Detector geometries and sizes.

C. Single LED mount

A single mount for the LED was developed that allows for the adjustment of the LED-detector distance. A single 540 nm LED strip was mounted on a printed circuit board and then integrated with three identical detectors (S1226), 2.7, 4.96 and 10.8 mm from the LED (center to center distance), respectively. The LED was driven at 20 mA with a total output power of 1 mW. The entire assembly was tested in 12 tissue mimicking liquid phantoms (A1-D3) with optical properties ranging from 0.1403 – 8.6725 cm^{-1} for absorption coefficient and 4.79 – 15.71 cm^{-1} for reduced scattering coefficient.

MC forward modeling was performed for comparison with the measured data. As shown in Table 8, the experimental data match relatively well with the simulated data (Measured/Sim close to 1.0) at the first center to center separation of 2.7 mm. At the second and third separations, the 540 nm LED did not produce sufficient signal to be detected in the darker phantoms. However, for the lighter phantoms that had sufficient signal, the measured data still matched relatively well with the simulated data. From this experiment, we found that a center-to-center distance greater than 5-mm is too large. For future iterations and designs, we know to keep the LED to detector separation to less than 3-mm so that the SNR can be maximized.

Table 8. MC forward modeling with measured data.

Phantom #	Phantom Optical Properties (μ_a , μ_s')	Measured/Sim SDS=2.7mm	Measured/Sim SDS=4.96mm	Measured/Sim SDS=10.8mm
A1	0.1403, 4.79	0.97	1.00	1.00
B1	0.1403, 7.98	0.81	0.95	1.25
C1	0.1403, 12.76	1.00	1.17	1.38
D1	0.1403, 15.95	0.95	1.13	1.20
A2	1.5343, 4.77	1.21	1.07	0.51
B2	1.5343, 7.96	1.05	1.10	0.93
C2	1.5343, 12.73	1.06	1.00	0.00
D2	1.5343, 15.91	1.11	1.12	0.00
A3	8.6725, 4.71	1.29	0.00	0.00
B3	8.6725, 7.85	1.27	0.00	0.00
C3	8.6725, 12.57	1.36	55.26	0.00
D3	8.6725, 15.71	1.49	112.15	0.00

D. Multi-LED-detector probe platform

Several monolithic LED-detector systems were also designed and implemented. The custom printed board layout was designed and Au plated to allow the ease of wire-bonding. An example of these systems is shown in Figure 7 where a schematic of the layout and the partially finished platform is shown. Six LEDs were mounted on the PCB board on the two sides of a 2.4 x 2.8 mm^2 photodiode (S1227). Due to the relatively low emission power at 420 nm, two LEDs at this wavelength are used. The LEDs and detector were wired to a 15-pin D connector on the same board, through which and a cable the PCB is connected to another driver PCB. The driver PCB provides current to each LEDs and an interface to a current amplifier. Currently, the device is under test for throughput and SNR. The forward and inverse MC model will also be adapted to simulate rectangular light sources and detectors.

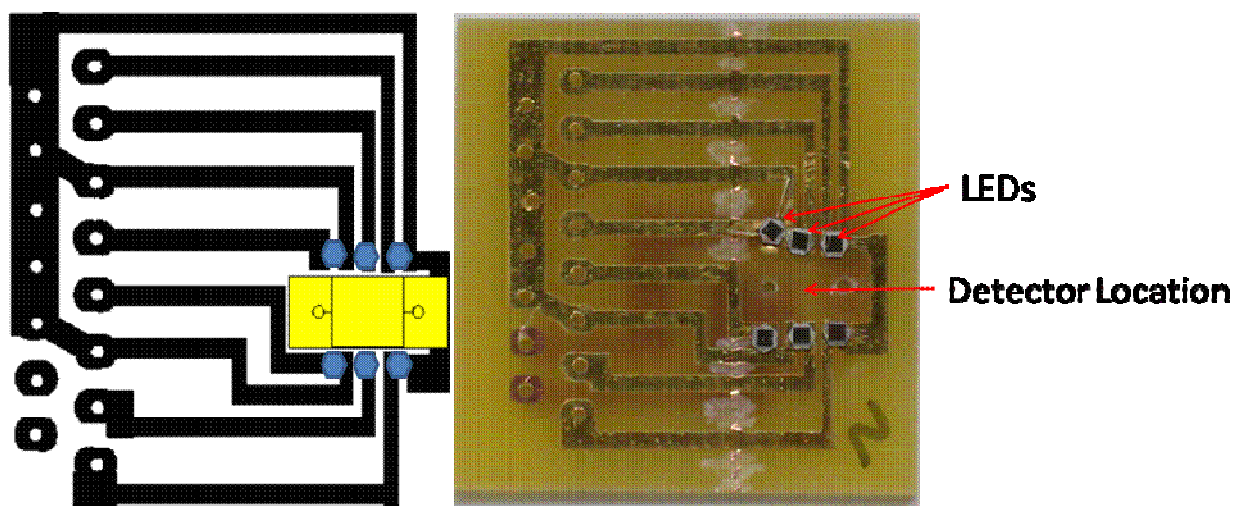


Figure 7. Monolithic LED and Detector system.

2.2. Project 2: Synthesis of contrast agents for molecular imaging

Statement of work for year 2

Synthesis of contrast agents for molecular imaging. Gold nanoparticles will be prepared via citrate reduction of chloroauric acid. The particle size will be adjusted to preferentially scatter NIR light. Anti-HER2 and anti-EGFR antibodies will be conjugated to the gold. The scattering spectrum of (1) the pre-labeled nanoparticles will be measured to verify their NIR resonant scattering properties and (2) the labeled nanoparticles to verify binding with the antibodies (a characteristic red-shift in the peak is expected to occur after binding) (year 2).

Accomplishments in year 2

The research accomplishments of year 2 have changed from what was originally proposed. While the focus still remains on using contrast agents for detection of breast cancer, a fluorescent contrast agent rather than a scattering contrast agent was explored since the former has higher signal to background in the red-near infrared. The contrast agent used toward this goal has been aminolevulinic acid (ALA) induced protoporphyrin IX (PpIX). We have successfully utilized ALA to induce PpIX production in four breast cell lines, as verified by an increase in fluorescence intensity and fluorescence lifetime over the normal cells. The most important finding of this work is the PpIX fluorescence contribution to the overall PpIX and autofluorescence signal, typically not reported, has shown to be an indicator of malignancy and could potentially be clinically relevant.

There is also a paper in preparation regarding the use of optical spectroscopy for monitoring tumor oxygenation and metabolism (see Appendix.)

2.2.1 ALA induced PpIX as a contrast agent

Initially, targeted gold nanoparticles were chosen as contrast agents, but ALA was found to be a more biocompatible option since it is produced in cellular mitochondria and can function as a therapeutic agent as well as a contrast agent when added exogenously. The prodrug aminolevulinic acid (ALA) has been proven to induce an overproduction of the fluorescent porphyrin molecule, PpIX, in malignant tissue [3]. PpIX is excited at 405 nm and emits in the NIR (635 nm) eliciting a photochemical reaction forming singlet oxygen resulting in cellular necrosis and inducing apoptosis [4]. The addition of exogenous ALA bypasses

this control, and lower amounts of ferrochelatase in malignant tissue cause a greater accrual of PpIX and delination from normal.

A. Cell study design

Four mammary cell lines with varying phenotype were chosen for this study: MCF10A (normal human mammary cells), MCF10 R-ras (transfected normal MCF10A cells with the R-ras removed from the phenotype), MDA-231 (undifferentiated malignant human mammary cells), and T47D (well-differentiated malignant human mammary cells). Baseline images (0 Hour) were acquired prior to treatment in culture media prior to treatment with ALA or buffered media. In experimental trials, the original culture media was removed and a 500 $\mu\text{g/mL}$ mixture of ALA was dissolved in culture media immediately buffered with Hepes buffer to approximately pH 6.8-7.2. The cells were allowed to incubate for 2 hours and then imaged. The cell plates were incubated for 2 more hours and imaged again for a total of 4 hours of incubation. The 500 $\mu\text{g/mL}$ concentration of ALA and 4 hour time trial was chosen because of its proven efficacy and ability to be directly compared to previous studies [2, 5, 6, 7]. In control experiments, the original cell media was removed and fresh culture media buffered to pH 6.8-7.2 was added and imaged concurrently with experimental trials. A total of ten experimental cell plates were imaged with 3 spots randomly chosen on the plates at each time point ($10 \times 3 = 30$ spots per time point). Five control cell plates were imaged with 3 spots randomly chosen on the plates at each time point ($5 \times 3 = 15$ spots per time point). After imaging, trypan blue was added to each plate to confirm cell viability. All images were acquired with a multiphoton laser scanning microscope (MPLSM). Lifetime images were collected with a fast photon-counting detector (H7244, Becker & Hickl) and time-correlated single photon counting electronics (SPC-730, Becker & Hickl) for high sensitivity [5].

Fluorescence lifetime imaging (FLIM) techniques quantify the time it takes for a fluorophore in the excited state to decay to its original state. These techniques are independent of fluorophore concentration, unlike intensity techniques, and can give information on molecular conformation or the local cellular environment [6]. The lifetime of a fluorophore is directly affected by its microenvironment, such as changes in temperature, pH, or oxygenation can increase or decrease the fluorescent lifetime values within a cell [6].

A. Localization of PpIX as determined by FLIM

Figure 8 shows representative multiphoton FLIM images of PpIX lifetime values for all four cell lines after 4 hours of ALA immersion. This figure qualitatively shows the differences in PpIX lifetimes and distribution among all of the cell lines. The scale differs between cell lines to allow for better lifetime visualization. The normal cell line, MCF10A, does not have an even distribution of PpIX. At 4 hours, approximately 5 ns lifetime values surround the nucleus and longer lifetimes are sporadically more distal. The transfected cell line, MCF10 R-ras has more PpIX present and a granular distribution throughout the cytoplasm. MDA-231, an undifferentiated malignant line, also has granular PpIX distribution at 4 hours, but appears to have longer lifetimes located in distal regions of the cell. T47D, a differentiated malignant cell line, shows an overall distribution of PpIX which appears granular and more evenly distributed throughout the cell. Because PpIX distribution is varied within each cell line it could result in different lifetimes (due to the dissimilar microenvironments). The T47D cell lines show PpIX accumulation in the same distribution as Shu-Min et al and Ji *et al* [7]. However, MCF10A, MCF10 R-ras and MDA-231 show PpIX accumulation more localized in distinct cellular regions. Ji et al found that the efficacy of PDT was related to the intracellular localization of the PpIX and distal lipophilic regions were found to be better [8].

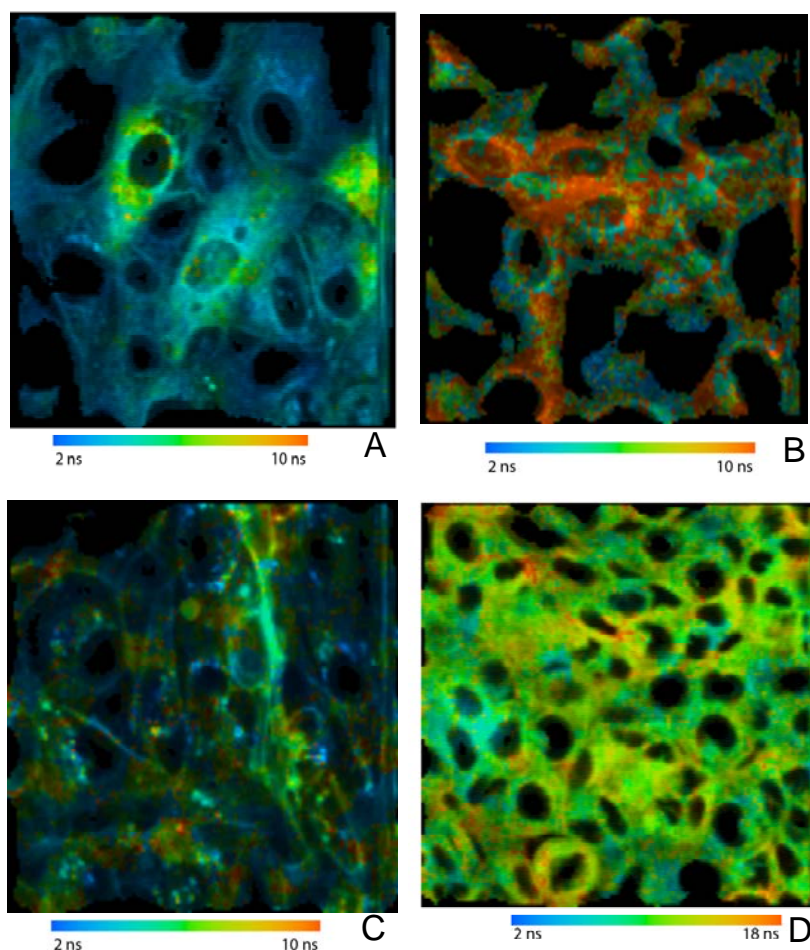


Figure 8. PpIX lifetime at 4 hours for all cell lines, MCF10A (A), MCF10 R-ras (B), MDA-231 (C) and T47D (D).

B. Fluorescence Lifetime

Table 9 shows the average and standard deviation of lifetime values of experimental PpIX (left columns) and bound NADH (right columns) for the control at 0, 2, and 4 hours. Experimental MCF10A and T47D PpIX lifetimes increase by a large amount over 4 hours, but MCF10 R-ras and MDA-231 do not increase after Hour 2. The value of PpIX lifetime does not exhibit a greater increase in all malignant cells (MCF10 R-ras and MDA-231) as compared to normal (MCF10A). Statistical analysis was completed to compare the control lifetime values (Bound NADH) to that of the experimental (PpIX). It was found that for all cell lines a statistically significant difference ($p < 0.05$) was seen between the Experimental and Control groups at hours 2 and 4. The fluorescence lifetime is indicative of the internal environment within a cell and the value can be influenced by many factors, i.e. intracellular pH, the molecules it is bonded with, and intracellular oxygenation. The T47D cell line, a differentiated malignant line has the longest PpIX lifetime at 15.4 ns; this value is similar to the monomeric form of PpIX in buffer [9]. The MCF10A cells, a normal breast cell line, exhibit the second longest lifetime at 5.0 ns. This lifetime is shorter than the monomeric form of PpIX found by Kress et al [10] in normal rat epithelial cells, but longer than the aggregate form. The MCF10 R-ras, a transformed MCF10A cell line, lifetime was 3.6 ns. MCF10 R-ras is a malignant transfection of MCF10A and proliferated more quickly than the MCF10A cell line and could have been in a different cell phase during these experiments causing a difference in lifetime. Finally, the MDA-231 cell line, an undifferentiated malignant breast cell line, had the shortest PpIX lifetime at 2.6 ns. This could be due to the microenvironment of the cell of the PpIX. The MDA-231 cell line has the PpIX mainly located at the distal ends of the cells whereas the T47D is more evenly spread through the cytoplasm. The small

distribution area, close proximity of the molecules and large distance from the perinuclear mitochondria mean that the oxygen environment of PpIX in the MDA-231 cell line could be different than the other cell lines. Other possible influences to lifetime include receptor status and protein mutation.

Table 9. Average and standard deviation of lifetime values.

Lifetime of cells - Long Component (ns)							
Experimental Group – PpIX Lifetime				Control Group – Bound NADH Lifetime			
	0 Hour	2 Hour	4 Hour		0 Hour	2 Hour	4 Hour
MCF10A*	2.6 ± 0.2	3.4 ± 0.8	5.0 ± 3.4	MCF10A Control	2.7 ± 0.2	2.7 ± 0.2	2.7 ± 0.1
MCF10 R-ras*	2.5 ± 0.2	3.8 ± 0.9	3.7 ± 0.8	MCF10 R-ras Control	2.4 ± 0.3	2.4 ± 0.2	2.2 ± 0.3
MDA-231*	2.1 ± 0.1	2.8 ± 0.5	2.6 ± 0.5	MDA231 Control	2.1 ± 0.0	2.1 ± 0.2	2.2 ± 0.3
T47D*	2.7 ± 0.1	13.5 ± 0.8	15.4 ± 1.8	T47D Control	2.6 ± 0.1	2.6 ± 0.2	2.5 ± 0.1

Average and standard deviation of lifetime values at the baseline, 2 and 4 hours of all four cell lines after immersion in ALA and culture media (experimental) or culture media (control). Asterisks denote statistically significant ($p < 0.05$) difference between Experimental and Control Groups at 2 and 4 Hours.

Table 10 is a comparison table of the large range of PpIX lifetimes found in previous literature studies in similar systems. The table lists buffer solution and biological systems in which PpIX lifetime was calculated. Asterisks denote exogenous PpIX addition instead of ALA-induced PpIX. The hours of immersion are shown after the biological systems. The RR1022 cells are normal rat epithelial cells. The values in this study are within the range of reported values in varying biological systems.

Table 10. PpIX Comparison Table.

Biological System or Solvent	Lifetime
Buffer (bi-exponential monomer)* [9]	1.5 & 15.8
RR1022 cells (aggregate) – 5 hours [10]	3.6
RR 1022 cells (monomer) – 5 hours [10]	7.4
Chicken Embryo (aggregate) – 6 hours [11]	5.2
Chicken Embryo (monomer) – 6 hours [11]	15-20

C. Contribution of PpIX

Figure 9 is a line graph showing how the relative contribution of PpIX to the overall experimental signal changes over time. The experimental signal consisted of autofluorescent NADH, which has a bound and free form separable by lifetime, and a PpIX fluorescence signal. The percent contribution is a relative value comparing the contribution of bound NADH to PpIX after the free NADH has decayed to less than 0.5%. The error bars shown on this graph are the standard deviations of the contributions at the 2 and 4 hour time points. The variation appears to be greater at the 4 hour time point as compared to the 2 hour time point. The 0 hour time point represents the baseline measurement prior to cellular immersion in ALA. This figure shows that the contribution of the PpIX signal is significantly greater in all of the malignant cell lines as compared to the normal cell line (as denoted by the asterisks next to the malignant cell lines in the legend.) The kinetics of lifetime contribution show that the contribution of PpIX relative to bound NADH stops increasing after 2 hours, which is important because intensity and lifetime keep changing after this time. The PpIX lifetime contribution could be used to differentiate normal and malignant cells sooner after ALA treatment than intensity measurements, thus decreasing the time between ALA treatment and laser therapy [3]. Most importantly the PpIX lifetime contribution is an indicator of malignancy in these cell

studies that can be used for diagnosis. Further cell studies will be utilized to investigate the influence of receptor status on PpIX localization, PpIX lifetime and PpIX contribution in breast cell lines.

Kinetics of Contribution of PpIX

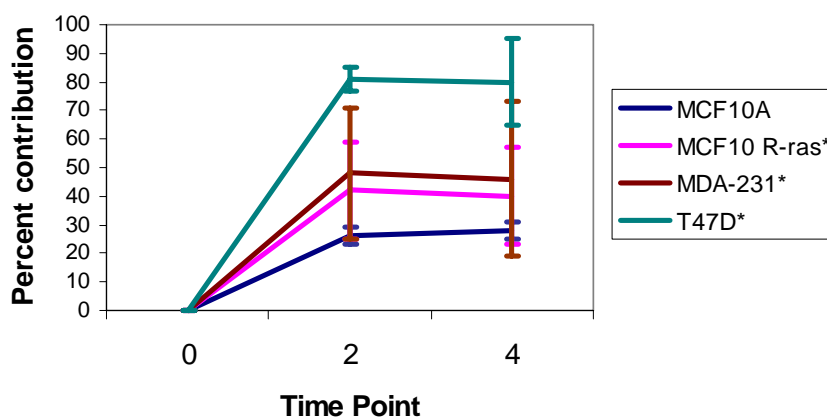


Figure 9. Average and standard deviation of the percent contribution of the lifetime over 4 hours. Asterisks denote all malignant cell lines are statistically different from normal (MCF10A) at 2 and 4 hours from baseline ($p < 0.05$).

3. KEY RESEARCH ACCOMPLISHMENTS

During the last 12 months, the following major achievements have been accomplished:

PROJECT 1

1. Building single-pixel probes P3-1 (600 μm fiber adjacent to an edge-trimmed 1.0 mm^2 detector), P3-2 (1.0 mm fiber adjacent to an edge-trimmed 2.4 \times 2.4 mm^2 detector), P4-1 (600 μm fiber in the center of a 2.4 \times 2.4 mm^2 detector) and P4-2 (1.0 mm fiber in the center of a 2.4 \times 2.4 mm^2 detector), as shown in Figure 1;
2. Test of P3-1 and P3-2 in synthetic tissue phantoms with know optical properties and comparing the experimental diffuse reflectance spectra with those of a forward MC model.
3. Extraction of phantom optical properties from diffuse reflectance spectra using an inverse MC model.
4. Extracting phantom optical properties with reduced number of wavelength and comparing the performance with that of the bench-top system with all wavelengths.
5. Design and building the first generation system-on-a-chip single-channel device

PROJECT 2

1. This study established that localization of PpIX is cell line dependent.
2. PpIX lifetime is not indicative of malignancy and that has not been shown previously.
3. The contribution of PpIX to the fluorescent signal, correlated with malignancy in this study.
4. Paper in preparation regarding the use of optical spectroscopy for monitoring tumor oxygenation and metabolism, see Appendix.

4. REPORTABLE OUTCOMES

- Millon, SR, Provenzano, PR, Elicieri, KW, Brown, JQ, Keely, PJ, Ramanujam, N. “Comparison of the effect of 5-aminolevulinic acid on the PpIX induced fluorescence intensity and lifetime of normal and malignant breast cell lines.” ECI: Advances in Optics for Biotechnology, Medicine and Surgery. (2007).
- Millon, SR, Elicieri, KW, Keely, PJ, Ramanujam, N. “Lifetime of 5-aminolevulinic acid induced protoporphyrin IX.” In Preparation.
- Palmer, G.M., R.J. Viola, T. Schroeder, P.S. Yarmolenko, N. Ramanujam, M.W. Dewhirst. “Use of optical spectroscopy for the characterization of tumor oxygenation and metabolic redox ratio.” Poster presentation, International Congress of Radiation Research, San Francisco, CA, July 2007.
- Palmer, GM, Viola, RJ, Schroeder, T, Yarmolenko, PS, Dewhirst, MW, Ramanujam, N. “Use of optical spectroscopy to monitor tumor physiology.” In Preparation.

5. CONCLUSIONS

PROJECT 1

As described previously, we have built single pixel probes P3-1, P3-2, P4-1, and P4-2, and we are currently characterizing and evaluating them for signal-to-noise ratio and capability for accurate MC model inversions on synthetic tissue phantoms with known optical properties. We have determined that there is good reproducibility in our measurements with probe P3-2 and promising phantom inversion results. This shows the feasibility of creating an optical spectral imaging system based on a tunable source and silicon detectors. We have determined that it is possible to extract optical properties even when the number of wavelengths is reduced to 5 (as opposed to 41 used in the bench-top system). We have also begun to characterize the single-pixel device for signal-to-noise ratio and have done some MC forward-modeling to test the feasibility of using LEDs as our light source. Once we have characterized the single-pixel device, we can continue to iterate through our design and create a multi-pixel spectral imaging system in the near future. We hope this research will significantly reduce the cost, size and complexity of the current optical spectroscopy technologies.

PROJECT 2

The addition of exogenous 5-aminolevulinic acid (ALA) induces a production of excess protoporphyrin IX (PpIX) in cells. The accumulation of ALA can be relatively quantified with fluorescence intensity. Fluorescence lifetime imaging provides information about the photosensitizer microenvironment independent of concentration. This study found that all cell lines showed a significant increase in PpIX lifetime at 2 and 4 hours of ALA immersion compared to cellular autofluorescence lifetimes. The differentiated malignant cell line, T47D, has the greatest average lifetime, 15.4 ns, and the normal, MCF10A, cell line was second longest, 5 ns after 4 hours of ALA immersion. The undifferentiated malignant cell line, MDA-231 has the smallest average lifetime, 2.6 ns and transfected MCF10 R-ras had a lifetime of 3.7 ns. The differences in lifetime indicate different cellular environments, but the mechanism behind this is still unknown. Lifetime values correlated to the fluorescent intensities of each cell line at all time points. However, the contribution to the decay curve from PpIX related to the malignancy of the cell line at 2 and 4 hours. All malignant cell lines had significantly greater contribution from PpIX than the normal cell line with ALA treatment. Lifetime values have been previously explored, but studies have overlooked respective contributions. PpIX contribution in a biological system should be included in lifetime studies as it serves as an indicator of malignancy.

6. REFERENCES

1. Palmer, G., Ramanujam, N, *Monte Carlo-based inverse model for calculating tissue optical properties. Part 1: Theory and validation on synthetic phantoms*". Applied Optics, 2006. **45**(5).
2. Zhu, C., et al., *Use of a multiseparation fiber optic probe for the optical diagnosis of breast cancer*. J Biomed Opt., 2005. **10**(2): p. 024032.
3. Andersson-Engels, S., et al., *Preliminary evaluation of two fluorescence imaging methods for the detection and the delineation of basal cell carcinomas of the skin*. Lasers Surg Med, 2000. **26**(1): p. 76-82.
4. Hirschberg, H., et al., *ALA- and ALA-ester-mediated photodynamic therapy of human glioma spheroids*. J Neurooncol, 2002. **57**(1): p. 1-7.
5. Utzinger, U., et al, *Performance estimation of diagnostic tests for cervical precancer based on fluorescence spectroscopy: effects of tissue type, sample size, population, and signal-to-noise ratio*. IEEE Trans Biomed Eng, 1999. **46**(11): p. 1293-303.
6. Lakowicz, J.R., *Principles of Fluorescence Spectroscopy*. 3rd ed. 2006, New York: Springer.
7. Shu-Min, W., et al., *Photodynamic Effects of 5-aminolevulinic acid and its hexylester on several cell lines*. Acta Biochimica et Biophysica Sinica, 2003. **35**(7): p. 655-660.
8. Ji, Z., et al., *Subcellular localization pattern of protoporphyrin IX is an important determinant for its photodynamic efficiency of human carcinoma and normal cell lines*. J Photochem Photobiol B, 2006. **84**(3): p. 213-20.
9. Brancalion, L., et al., *Characterization of the photoproducts of protoporphyrin IX bound to human serum albumin and immunoglobulin G*. Biophys Chem, 2004. **109**(3): p. 351-60.
10. Kress, M., et al., *Time-resolved microspectrofluorometry and fluorescence lifetime imaging of photosensitizers using picosecond pulsed diode lasers in laser scanning microscopes*. Journal of Biomedical Optics, 2003. **8**(1): p. 26-32.
11. Schneckenburger, H., et al., *Time-resolved in-vivo fluorescence of photosensitizing porphyrins*. J Photochem Photobiol B, 1993. **21**(2-3): p. 143-7.

7. APPENDIX

Use of optical spectroscopy to monitor tumor physiology

Gregory M. Palmer¹, Ronald J. Viola¹, Thies Schroeder¹, Pavel S. Yarmolenko¹, Mark W. Dewhurst¹, Nirmala Ramanujam²

Duke University

¹Dept. Radiation Oncology

²Dept. Biomedical Engineering

Abstract

This study demonstrates the use of optical spectroscopy for monitoring tumor oxygenation and metabolism. Hemoglobin saturation and redox ratio were quantified for a set of 14 and 9 mice, respectively, and showed consistent changes upon carbogen breathing. Both paired ($p < 0.005$) and unpaired ($p < 0.005$) t-tests on the combined data showed highly significant increases in hemoglobin saturation. The redox ratio was measured at the start and end of each experiment, and 8 of 9 mice showed an increase in this metric, and these changes were again significant using a paired t-test ($p < 0.005$). The magnitude of the change in hemoglobin saturation was highly correlated with that of the redox ratio ($r = 0.88$, excluding one outlier). These data were compared to that obtained concurrently using an established invasive technique, the Oxylite pO_2 system, which showed an increase in pO_2 at a lower significance level ($p < 0.05$). Optical spectroscopy measurements are demonstrated to provide a reliable, reproducible indication of changes in tumor physiology.

Introduction

Tumor oxygenation is a critical factor in determining the efficacy of radiation and chemotherapy in cancer. Hypoxia leads to genomic instability, and resistance to radiation, chemotherapy, and photodynamic therapy [1]. Martinive et al. recently demonstrated that intermittent hypoxia in particular can induce radiation resistance both *in vitro*, and *in vivo* [2]. The ability to monitor tumor oxygenation dynamically *in vivo* would thus be of tremendous importance in determining prognosis, and potentially in guiding therapy.

In vivo measurement of tissue oxygenation are most commonly performed using needle-based sensors, including the Clark-type electrode, and fluorescence lifetime sensors, such as the OxyLite pO₂ system [3]. These approaches are capable of providing accurate, absolute measurements of oxygen tensions, however such devices have a number of limitations. They have a small sampling area on the order of 0.038 mm² (Oxylite) or 80 μm² (Clark-type electrode) [3]. This can be an advantage if local information is desired, but it is difficult to generalize one or a few measurement points to a global picture of tumor physiology. These devices also require the diffusion of oxygen into the sensor, which results in a stabilization period of around 15 minutes for the Oxylite sensor, which can cause difficulties when measuring dynamic changes in pO₂ in a living subject, where fluctuating pO₂ and motion artifacts could cause significant problems.

Optical spectroscopy has recently been explored as a tool for monitoring the physiological effects of chemotherapy in clinical breast cancer treatment in several case studies and pilot studies [4-7]. Finlay and Foster demonstrated the use of diffuse reflectance spectroscopy for measuring hemoglobin saturation in proof-of-principle measurements of murine tumor tissue in response to carbogen and nitrogen breathing [8]. These collective studies showed that optical spectroscopy is capable of monitoring changes in tumor physiology in response to various treatments, however they do not compare their measurements in a systematic way to any other established technique. The goal of this study is to monitor changes in oxygenation in response to carbogen breathing using both optical spectroscopy, and an established method of measuring tumor pO₂, the

Oxylite pO₂ system to establish optical spectroscopy as a viable means of monitoring tumor physiology.

Methods

Murine mammary carcinoma cells of the 4T1 cell line were injected into a set of 14 athymic NCr nu/nu mice (NCI-Fitzpatrick). **Xxx** cells were injected into the flank of each mouse, and the tumors were allowed to grow until they reached a size of approximately 1.0 cm diameter (around 1.5 weeks). Upon reaching the proper size, the mouse was anesthetized with **xxx** mg/kg Pentobarbital, and the mouse was placed on a warming blanket. The optical spectroscopy probe and Oxylite sensors were then positioned on the surface of the tumor, which the spectroscopy probe placed in contact with the surface of the skin overlaying the tumor, and two Oxylite sensors being inserted into the tumor on either side of the spectroscopy probe. Fig. 1 shows the experimental setup. A baseline reading was established for a period of at least 15 minutes to allow the Oxylite sensors to stabilize and baseline spectroscopy measurements to be acquired. Then, the mouse was administered carbogen gas (95% O₂, 5% CO₂) at a rate of 5 L/min for the duration of the experiment. Diffuse reflectance measurements were then acquired every minute for the first 10 minutes, and every 5 minutes thereafter for up to 90 minutes, or until the measurements stabilized. Fluorescence measurements were made at baseline, and at the end of the experimental time period. At the end of the experiment each mouse was sacrificed using an overdose of Pentobarbital.

Optical spectroscopy measurements were made via a fiber optic probe coupled to the Skinskan (J.Y. Horiba, Edison, NJ) fluorometer, which have been described extensively in previous publications [9, 10]. Briefly, the fiber optic probe consists of a

central collection core of 31 fibers with a diameter of 1.52 mm surrounded by an illumination ring, also with 31 fibers, having an outer diameter of 2.18 mm. The Skinskan consists of a 150 W xenon arc lamp, double excitation/emission monochromators, and a photomultiplier tube detector. Optical spectroscopy measurements were made by placing the fiber optic probe in direct contact with the tissue surface. Two sets of optical measurements were made, (1) the diffuse reflectance spectra (350-600 nm), and (2) the fluorescence emission spectra obtained at 350 and 460 nm excitation, which excite NADH and FAD, respectively.

Concurrent with the optical measurements, the tissue pO₂ was determined using the Oxylite pO₂ sensor (Oxford Optronics). This system consists of a needle-based sensor consisting of containing a platinum-based fluorophore enclosed in a silicone matrix. This fluorophore is quenched by oxygen, and the resulting change in lifetime is used to quantify the pO₂ of the surrounding tissue. This sensor was inserted into the superficial region of the tumor at a depth of approximately 1-3 mm, to correspond roughly to the sensing depth of the optical spectroscopy measurement.

The diffuse reflectance data were then processed using a Monte Carlo-based model of diffuse reflectance to extract the physiological information related to the absorption and scattering properties of the tissue [9]. Briefly, the model works by constraining the absorption and scattering to be due to specific known absorbers and scatterers in the tissue. The absorption (μ_a) and reduces scattering (μ_s') coefficients of the medium can then be calculated based on these properties of the absorbers and scatterers. The optical properties are then fed into a Monte Carlo model of diffuse reflectance to determine what the collected diffuse reflectance would be given those optical properties

for the specific measurement geometry employed. A nonlinear least squares algorithm is then used to minimize the difference between the measured and simulated diffuse reflectance spectra, and the resulting absorber and scatterer properties are returned as the output of the algorithm. In this case, three absorbers were used: oxy and deoxy hemoglobin (Hb) and a baseline skin absorption spectrum, i.e. the absorption of skin in the absence of blood and melanin [11]. Scattering was approximated using Mie theory, using a single size scatterer having a range of sizes between 0.35 and 1.5 μm , which has previously been shown to be able to well approximate the scattering properties of a distribution of scatterer sizes expected in biological samples [9]. Hemoglobin saturation ($\text{HbO}_2 / (\text{Hb} + \text{HbO}_2)$) was then used to quantify the tissue oxygenation.

The fluorescence data were processed using another Monte Carlo-based model of fluorescence to separate the effects of absorption and scattering from the measured fluorescence spectra. Briefly, this algorithm uses Monte Carlo simulations, incorporating the excitation wavelength optical properties, to model the path light takes from the light source to the fluorophore. The intrinsic fluorescence properties then determine how much of this light will be converted to fluorescence. Finally, another Monte Carlo simulation, incorporating the emission wavelength optical properties, determines how much of this generated fluorescence returns to the tissue surface to be collected by the optical probe. Using a process described in detail elsewhere [12], it is possible to mathematically separate the intrinsic fluorescence properties from the simulated effects of absorption and scattering, to yield a quantity that is proportional to the product:

$$2.303\epsilon C \phi \eta(\lambda_m) \Delta\lambda \quad (1)$$

Where ε is the extinction coefficient of the fluorophore at the excitation wavelength, C is its concentration, ϕ is its quantum yield, λ_m is the emission wavelength, $\Delta\lambda$ is the measurement bandwidth, and η is the emission wavelength probability distribution for the fluorophore. The redox ratio was then taken as the ratio of $F_{460,525}/(F_{460,525}+F_{350,450})$, with $F_{460,525}$ being the intrinsic fluorescence emission at 460 nm excitation, 525 nm emission, which corresponds roughly to the FAD fluorescence emission maxima, while $F_{350,450}$ would correspond to the NADH emission maxima.

Results

Fig. 2 shows representative fits from a single mouse at baseline and after carbogen breathing. It can be seen that the alpha and beta bands of hemoglobin absorption at around 540 and 580 nm appear more distinct in Fig. 2(b), which is indicative of greater oxygenation. This corresponds to an increase in saturation from approximately 60% to 80%, as retrieved from the diffuse reflectance model. It can be seen that the fit provides a good approximation of the measured diffuse reflectance throughout the majority of the wavelength range, with larger errors seen closer to 600 nm. This discrepancy may be the result of approximations used in the model in describing the tissue as a homogeneous medium (see discussion).

Fig. 3 shows the tissue pO_2 obtained from each of the Oxylite probes and Hb saturation for a representative animal, with carbogen breathing beginning at $t=90$ minutes, and continuing for the duration of the experiment. It can be seen that the Hb saturation shows a more rapid response to the administration of carbogen at $t=90$ minutes, which was found to be typical of other mice as well. One Oxylite probe (top panel) showed no change in pO_2 upon administration of carbogen, which was a common

occurrence. Another interesting time course, which demonstrates measurement of fluctuant hypoxia is shown in Fig. 4, where it can be seen that both the hemoglobin saturation and pO_2 show similar fluctuations, with changes in Hb saturation again preceding those of the Oxylite pO_2 probe.

Fig. 5 shows the baseline, and stabilized carbogen breathing measurements. All measurements were generally stabilized after 10 minutes of carbogen breathing, so measurements were averaged after this time point to produce the carbogen-breathing data points. For the set of 14 animals, a significant increase was seen in pO_2 ($p < 0.05$) and Hb saturation ($p < 0.005$), these significance levels were identical for both paired and unpaired t-tests, which is indicative of the high degree of inter-animal consistency. Fig. 5(d) shows the redox ratio (FAD/(NADH+FAD) fluorescence) for the case before (blue) and after (red) carbogen administration, obtained for a subset of the animals in this study. This is the ratio of intrinsic fluorescence properties defined by equation 1. In the presence of oxygen, the redox ratio would be expected to increase [13], as is shown for eight of the nine cases. For the case where the redox ratio did not decrease, it is interesting to note that the Hb saturation also did not change significantly upon carbogen administration (mouse 5), so the data are consistent using two independent measures of tumor physiology. A paired t-test indicates that there is a significant increase in the redox ratio upon the administration of carbogen ($p < 0.005$), while the unpaired test is not significant owing to large inter-animal variability. Finally, Fig. 6 shows a scatterplot of the absolute change in redox ratio, plotted against the change in Hb saturation for each animal. It can be seen that these parameters are highly correlated, with the exception of one outlier

having a very large change in Hb saturation (mouse 13). These data have a correlation coefficient of 0.22 with the outlier, and 0.88 excluding it.

The reliability of these techniques was evaluated by examining how many of these animals demonstrated significant differences within each animal. All 14 mice showed an increase in hemoglobin saturation. For two of these, there were not enough usable measurements for significance testing, but 10 of the 12 remaining (83%) showed significant changes ($p < 0.01$). For the Oxylite pO_2 measurements, an additional 2 animals were excluded due to experimental difficulties with the sensors, but of the remaining 10 animals, 6 showed a significant increase in pO_2 ($p < 0.01$). Thus, there are significant differences in 60% of animals, versus 83% for hemoglobin saturation. However this difference is not statistically significant using a Chi-squared test for equality of distributions.

Discussion

The results presented here demonstrate that the use of optical spectroscopy is capable of providing highly reliable information regarding tissue physiology. In fact, it compared favorably an established approach, that of the Oxylite pO_2 sensor, which has been used previously to monitor tumor physiology in a number of preclinical and clinical studies (e.g. [14, 15]). A key limitation of the Oxylite sensor is its small sampling region, which makes it highly sensitive to positioning, and for cases where the Oxylite is positioned in a poorly perfused or necrotic microenvironment, the sensor accurately reports pO_2 close to zero throughout the experiment, as can be seen in around half of the mice (Fig. 5(a)). In fact, the two Oxylite sensors frequently reported pO_2 that differed from one another by a factor of 2 or more, as seen in Figs. 3-4, highlighting the difficulty

of using a few needle-based sensors such as these as an indicator of global tumor oxygenation due to the high degree of heterogeneity within a tumor. The optical measurement of hemoglobin saturation however, showed consistent results across all animals (see Fig. 5(b)), as reflected by the highly significant unpaired differences seen in the hemoglobin saturation ($p < 0.005$). The redox ratio also showed highly consistent relative changes upon administration of carbogen, however the high inter-animal variability may restrict the usefulness of this metric to paired comparisons. An advantage of using the redox ratio is that it may be indicative of changes in metabolic activity caused by factors other than tissue oxygenation, thus providing complementary information, however this was not tested here.

One potential concern is the ability of the optical probe to sample the tumor through the skin. Monte Carlo simulations of fluorescence indicate that the median probing depth (i.e. the median depth of origination for collected fluorescence), ranges from 0.4-2.8 mm for the range of optical properties representative of those encountered in this study. Typical thickness of the skin in these mice is around **0.5 mm**. This would suggest that the effect of the skin on the measurement could be significant, particularly for high absorption and low scattering. We are currently working on an optimized probe geometry, which will minimize any such artifact. We have also experimented with removing the skin, and obtained similar results to that with the skin intact, thus lending confidence to the current approach.

Another related concern is the use of a homogeneous model, when the skin and tumor layers are likely to have different optical properties. A two layer model could be employed in the future, but this would significantly complicate the modeling, and would

likely require a more complex measurement geometry to enable the effective separation of the optical properties of the two layers, using multiple source detector separations, or angularly resolve measurements, for example [16]. In this simplified case, the extracted optical properties represent some composite average of the two layers, and the best approach may be to design a probe that maximizes sampling volume, thus weighting this average more towards the deeper tumor tissue.

In conclusion, it has been demonstrated that optical spectroscopy can successfully monitor changes in tissue oxygenation in response to a perturbation. Future work will incorporate such measurements into preclinical and clinical studies examining the effects of anti-angiogenic therapy, chemotherapy, and radiation therapy upon tumor physiology, both as an indicator of therapeutic efficacy, and ultimately as a means of guiding therapy toward the most efficacious treatment regimen.

References

1. P. Vaupel and L. Harrison, "Tumor hypoxia: causative factors, compensatory mechanisms, and cellular response," *Oncologist*, 9 Suppl 5, 4-9, (2004).
2. P. Martinive, F. Defresne, C. Bouzin, J. Saliez, F. Lair, V. Gregoire, C. Michiels, C. Dessy, and O. Feron, "Preconditioning of the tumor vasculature and tumor cells by intermittent hypoxia: implications for anticancer therapies," *Cancer Res*, 66, 11736-44, (2006).
3. R. D. Braun, J. L. Lanzen, S. A. Snyder, and M. W. Dewhirst, "Comparison of tumor and normal tissue oxygen tension measurements using OxyLite or microelectrodes in rodents," *Am J Physiol Heart Circ Physiol*, 280, H2533-44, (2001).
4. A. Cerussi, D. Hsiang, N. Shah, R. Mehta, A. Durkin, J. Butler, and B. J. Tromberg, "Predicting response to breast cancer neoadjuvant chemotherapy using diffuse optical spectroscopy," *Proc Natl Acad Sci U S A*, 104, 4014-9, (2007).
5. B. J. Tromberg, A. Cerussi, N. Shah, M. Compton, A. Durkin, D. Hsiang, J. Butler, and R. Mehta, "Imaging in breast cancer: diffuse optics in breast cancer: detecting tumors in pre-menopausal women and monitoring neoadjuvant chemotherapy," *Breast Cancer Res*, 7, 279-85, (2005).
6. R. Choe, A. Corlu, K. Lee, T. Durduran, S. D. Konecky, M. Grosicka-Koptyra, S. R. Arridge, B. J. Czerniecki, D. L. Fraker, A. DeMichele, B. Chance, M. A.

- Rosen, and A. G. Yodh, "Diffuse optical tomography of breast cancer during neoadjuvant chemotherapy: a case study with comparison to MRI," *Med Phys*, 32, 1128-39, (2005).
7. D. B. Jakubowski, A. E. Cerussi, F. Bevilacqua, N. Shah, D. Hsiang, J. Butler, and B. J. Tromberg, "Monitoring neoadjuvant chemotherapy in breast cancer using quantitative diffuse optical spectroscopy: a case study," *J Biomed Opt*, 9, 230-8, (2004).
 8. J. C. Finlay and T. H. Foster, "Hemoglobin oxygen saturations in phantoms and in vivo from measurements of steady-state diffuse reflectance at a single, short source-detector separation," *Med. Phys.*, 31, 1949-59, (2004).
 9. G. M. Palmer and N. Ramanujam, "Monte Carlo-based inverse model for calculating tissue optical properties. Part I: Theory and validation on synthetic phantoms," *Appl Opt*, 45, 1062-71, (2006).
 10. G. M. Palmer, C. Zhu, T. M. Breslin, F. Xu, K. W. Gilchrist, and N. Ramanujam, "Monte Carlo-based inverse model for calculating tissue optical properties. Part II: Application to breast cancer diagnosis," *Appl Opt*, 45, 1072-8, (2006).
 11. R. Huang and S. Jacques, "Skin Optics Summary", 1998. Available: <http://omlc.ogi.edu/news/jan98/skinoptics.html>
 12. G. M. Palmer and N. Ramanujam, "Monte Carlo based Model to extract Intrinsic Fluorescence from Turbid media: Theory and Phantom Validation," *J Biomed Opt*, Submitted, (2007).
 13. B. Chance, B. Schoener, R. Oshino, F. Itshak, and Y. Nakase, "Oxidation-reduction ratio studies of mitochondria in freeze-trapped samples. NADH and flavoprotein fluorescence signals," *J Biol Chem*, 254, 4764-71, (1979).
 14. K. G. Brurberg, M. Thuen, E. B. Ruud, and E. K. Rofstad, "Fluctuations in pO₂ in irradiated human melanoma xenografts," *Radiat Res*, 165, 16-25, (2006).
 15. K. L. Blackwell, J. P. Kirkpatrick, S. A. Snyder, G. Broadwater, F. Farrell, L. Jolliffe, D. M. Brizel, and M. W. Dewhirst, "Human recombinant erythropoietin significantly improves tumor oxygenation independent of its effects on hemoglobin," *Cancer Res*, 63, 6162-5, (2003).
 16. Q. Liu and N. Ramanujam, "Experimental proof of the feasibility of using an angled fiber-optic probe for depth-sensitive fluorescence spectroscopy of turbid media," *Optics Letters*, 29, 2034-2036, (2004).

Figure Captions

Figure 1: Experimental setup used for these experiments. A single fiber optical probe was placed in contact with the skin overlaying the tumor, and two Oxylite sensors were placed on either side of it.

Figure 2: Representative diffuse reflectance fits at (a) baseline and (b) after carbogen breathing.

Figure 3: Representative time course data for showing pO_2 for each of the two Oxylite probes (top two panels), and the hemoglobin saturation. The animal was provided carbogen continuously after $t=90$ minutes, as indicated by the dashed line. Hemoglobin saturation and pO_2 for one of the Oxylite probes (middle panel) can be seen to increase with carbogen breathing. The other Oxylite probe shows no change upon carbogen breathing. This corresponds to mouse 8.

Figure 4: Time course demonstrating the measurement of fluctuant hypoxia for the two Oxylite probes (top two panels) as well as hemoglobin saturation. This corresponds to mouse 7.

Figure 5: The (a) hemoglobin saturation, (b) total hemoglobin, (c) pO_2 reported by the Oxylite system, and (d) redox ratio data for each of the mice in this study. The data were averaged for the baseline (black), and carbogen-breathing (white) levels.

Figure 6: Scatter plot of the change in hemoglobin saturation vs. the change in redox ratio. It can be seen that these are highly correlated, with the exception of one outlier having a large change in hemoglobin saturation, which corresponds to mouse 13.

Figure 1:

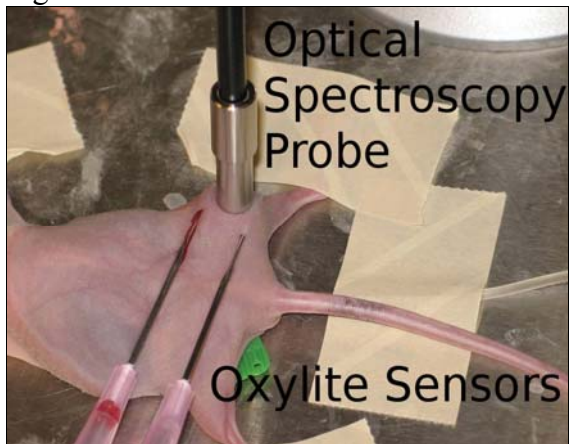


Figure 2:

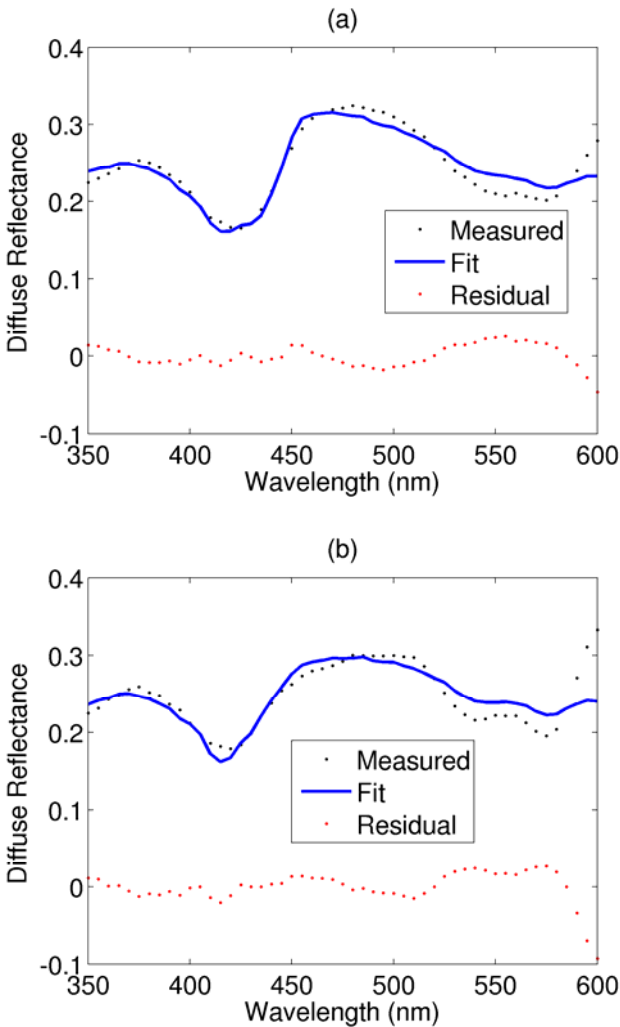


Figure 3:

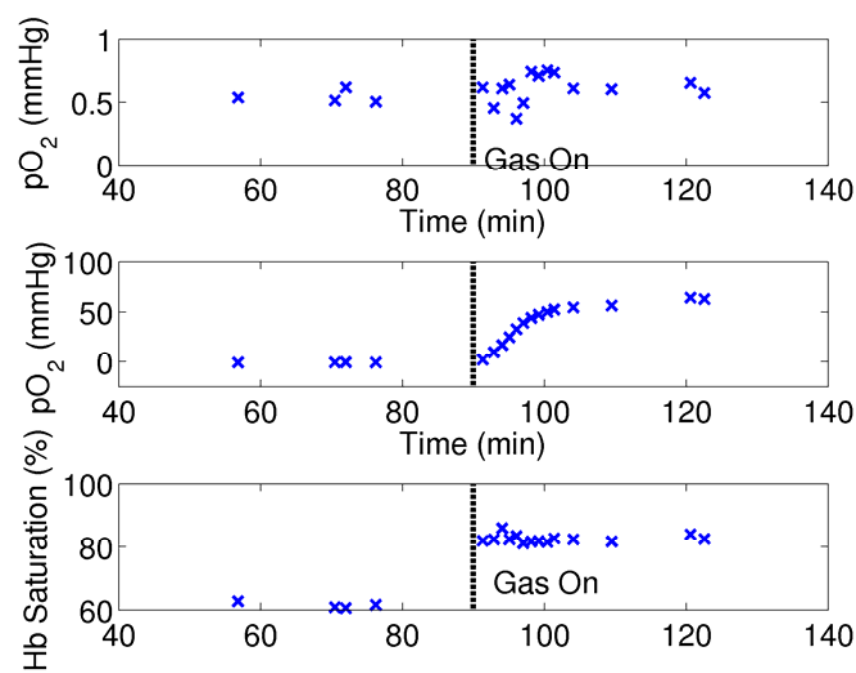


Figure 4:

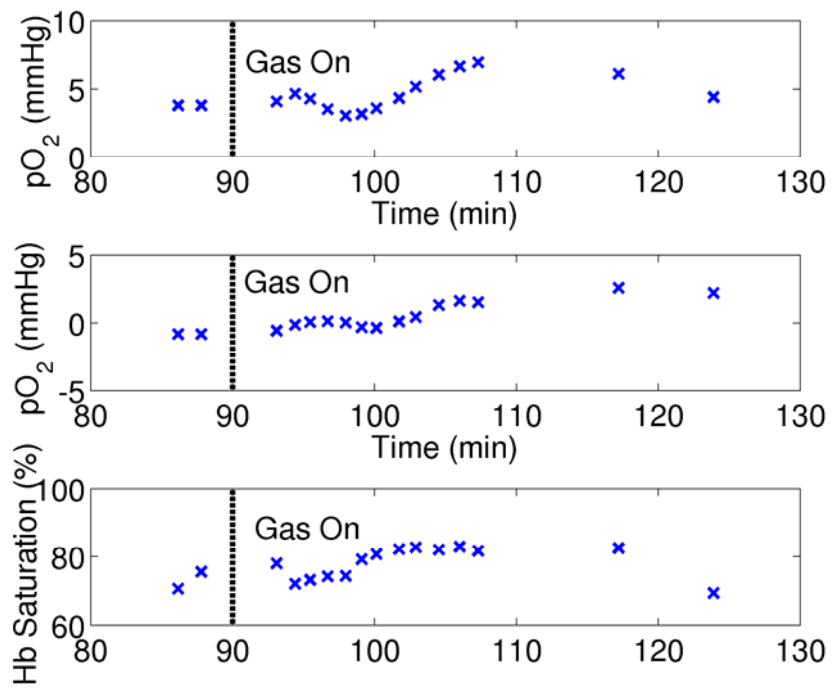
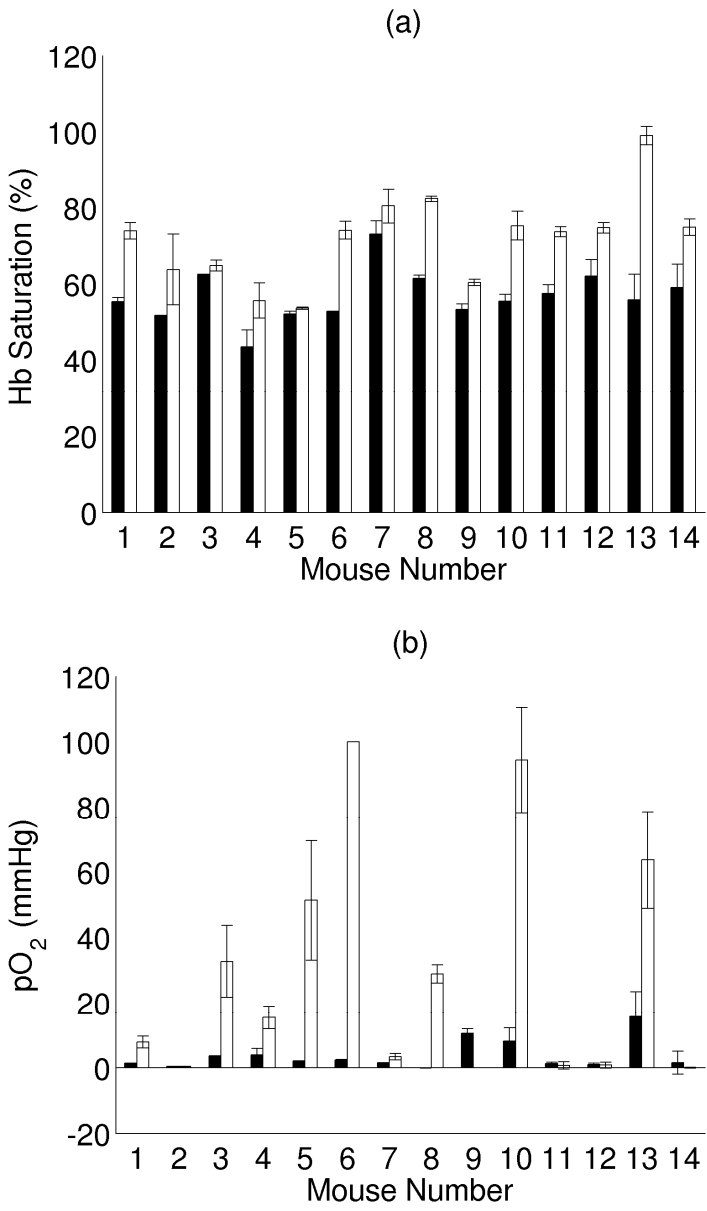


Figure 5:



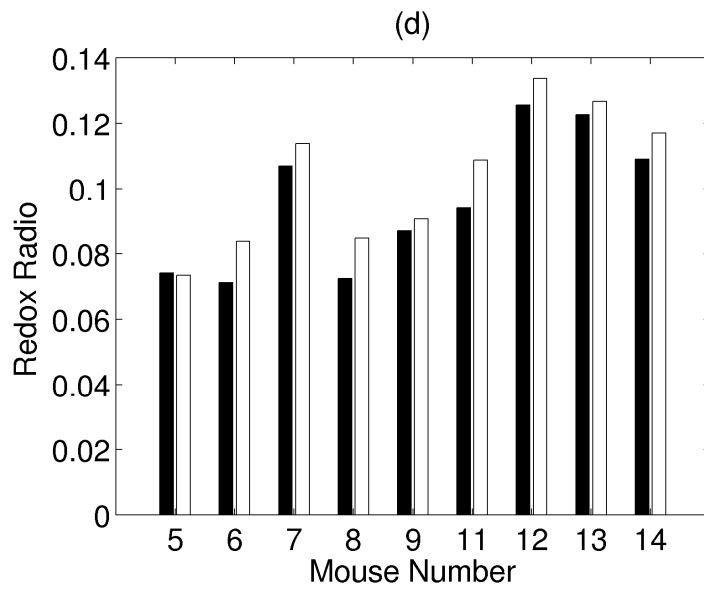
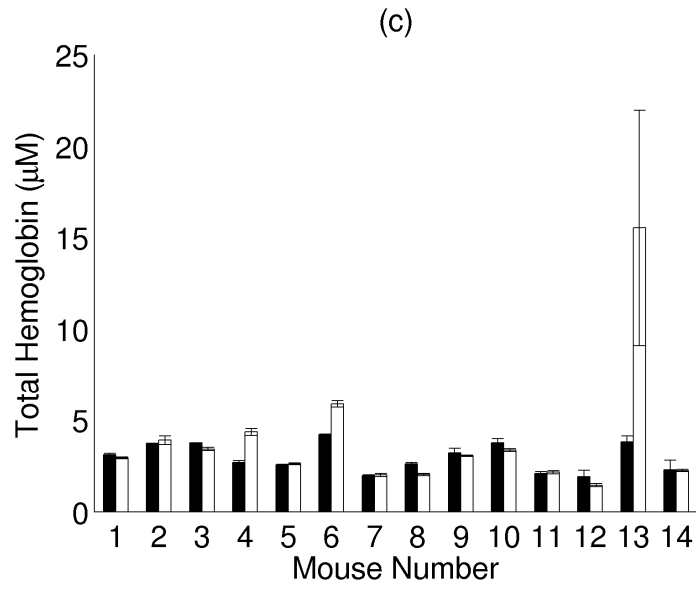


Figure 6:

